Colliding Ice Crystals in Turbulent Clouds

M Z Sheikh, K. Gustavsson, E. Lévêque, B. Mehlig, Alain Pumir, And A Naso

Colliding ice crystals in turbulent clouds

M. Z. Sheikh,[a,b] K. Gustavsson,[c] E. Lévêque,[d] B. Mehlig,[c] A. Pumir,[a] and A. Naso[d]

[a] *Univ Lyon, ENSL, CNRS, Laboratoire de Physique, F-69342 Lyon, France.*
[b] *Department of Mechanical Engineering, University of Engineering and Technology Lahore, 54890, Lahore, Pakistan.*
[c] *Department of Physics, Gothenburg University, 41296 Gothenburg, Sweden.*
[d] *Univ Lyon, CNRS, Ecole Centrale de Lyon, INSA Lyon, Univ Claude Bernard Lyon 1, Laboratoire de Mécanique des Fluides et d'Acoustique, UMR 5509, 69130, Ecully, France.*

ABSTRACT: Collisions, resulting in aggregation of ice crystals in clouds, is an important step in the formation of snow aggregates. Here, we study the collision process by simulating spheroid-shaped particles settling in turbulent flows, and by determining the probability of collision. We focus on plate-like ice crystals (oblate ellipsoids), subject to gravity, to the Stokes force and torque generated by the surrounding fluid. We also take into account the contributions to the drag and torque due to fluid inertia, which are essential to understand the tendency of crystals to settle with their largest dimension oriented horizontally. We determine the collision rate between identical crystals, of diameter $300\mu m$, with aspect ratios in the range $0.005 \leq \beta \leq 0.05$, and over a range of energy dissipation per unit mass, ε, $1\,\mathrm{cm}^2/\mathrm{s}^3 \leq \varepsilon \leq 250\,\mathrm{cm}^2/\mathrm{s}^3$. For all values of β studied, the collision rate increases with the turbulence intensity. The dependence on β is more subtle. Increasing β at low turbulence intensity ($\varepsilon \lesssim 16\,\mathrm{cm}^2/\mathrm{s}^3$) diminishes the collision rate, but increases it at higher $\varepsilon \approx 250\,\mathrm{cm}^2/\mathrm{s}^3$. The observed behaviors can be understood as resulting from three main physical effects. First, the velocity gradients in a turbulent flow tend to bring particles together. In addition, differential settling plays a role at small ε when the particles are thin enough (β small), whereas the prevalence of particle inertia at higher ε leads to a strong enhancement of the collision rate.

1. Introduction

As ice crystals collide in a turbulent cloud, they may stick to each other and coalesce to form larger aggregates (Pruppacher and Klett 1997). This process is an important ingredient in the growth of ice crystals and the formation of snow aggregates (Lo and Passarelli 1982; Mitchell 1988). Detailed field measurements have shown that the resulting aggregates have a characteristic exponential size distribution (Field and Heymsfield 2003), and are shaped approximately as prolate ellipsoids (Jiang et al. 2019). The determination of the probability of collision of ice-crystals appears as a crucial element in the quantitative description of this process (Khain and Pinsky 2018; Gavze and Khain 2022).

Among the collision processes involving hydrometeors, those between ice crytals appear to be the least understood (Wang 2013). Collisions between small droplets have been extensively studied theoretically and numerically over the past decades (Shaw 2003; Franklin et al. 2005; Falkovich and Pumir 2007; Ayala et al. 2008b,a; Grabowski and Wang 2013; Voßkuhle et al. 2014; Saito and Gotoh 2019). In the case of ice crystals, the complexity due to the particle anisotropy and to the possibility of crystals to settle with different orientations leads to fundamental difficulties. The settling of ice crystals was studied experimentally from field observations (Nakaya and Terada 1935; Matrosov et al. 2005) or tank measurements of idealized objects settling in a fluid (Willmarth et al. 1964). The first numerical investigations of settling ice crystals assumed a fixed horizontal orientation (major axis perpendicular to the gravity direction) (Pitter et al. 1973; Wang and Ji 1997). Hashino et al. (2014) imposed a steady flow around columns and plates with a fixed (but non-horizontal) orientation. More recently, it became possible to study numerically freely falling hexagonal ice plates (Cheng et al. 2015) and planar crystals of more complex shapes (Nettesheim and Wang 2018). All these studies were carried out in laminar flows (fixed uniform flow around a fixed particle, or particle settling in a fluid at rest). It also became possible to simulate numerically the settling of ice crystals in turbulence (Siewert et al. 2014a,b; Jucha et al. 2018; Naso et al. 2018; Gustavsson et al. 2021), and also to investigate numerically the collision of crystals in a turbulent flow (Siewert et al. 2014b; Gustavsson et al. 2017; Jucha et al. 2018; Gavze and Khain 2022). Experimentally, crystal-crystal collisions were mainly studied by considering small ice crystals colliding with a fixed ice or artificial target (Hosler and Hallgren 1960; Keith and Saunders 1989). More recent experiments focus on the aggregation efficiency (Connolly et al. 2012).

The goal of the present work is to provide an estimate of the collision kernel between settling ice crystals in turbulent flows. Notoriously, the turbulence intensity in clouds, as measured by the rate of dissipation of kinetic energy per unit mass, ε, varies over a wide range: from $\varepsilon \sim 1\,\mathrm{cm}^2/\mathrm{s}^3$ in weakly turbulent clouds up to $\gtrsim 10^3\,\mathrm{cm}^2/\mathrm{s}^3$ in cumulonumbi (Grabowski and Vaillancourt 1999).

Corresponding author: Alain Pumir, alain.pumir@ens-lyon.fr
Corresponding author: Aurore Naso, aurore.naso@ec-lyon.fr

We focus here on plate-like ice crystals. The convenient simplification, used here as well as in earlier works (Pitter et al. 1973), consists in approximating the crystal as a thin oblate spheroid. The density of the crystals, ρ_p is much larger than that of the surrounding fluid, ρ_f. We took here the same values as in Jucha et al. (2018), namely $\rho_p = 0.9194\,\mathrm{g/cm^3}$ and $\rho_f = 1.413\times10^{-3}\,\mathrm{g/cm^3}$. The description of anisotropic crystals requires an additional rotational degree of freedom, which affects the way the crystals sample the fluid. In particular, the settling velocity depends on the orientation of the crystal. This provides a mechanism that potentially enhances collision rate between crystals (Siewert et al. 2014b; Gustavsson et al. 2017; Jucha et al. 2018). Models that correctly capture the orientation dynamics of the settling crystals are therefore essential to reliably describe the collision processes. Determining the orientation dynamics and the settling velocity of ice crystals is also a crucial ingredient for the development of accurate numerical methods of cloud microphysics simulation (Shima et al. 2020).

Here, we consider very small crystals, with a semi-major axis $a = 150\mu$m. This size is smaller than the size of the smallest eddies in the flows considered. The modeling of the force and torque acting on such crystals is crucial for the present study. Recent experimental work (Lopez and Guazzelli 2017) has shown the importance of fluid inertia in determining the torque acting on crystals. This aspect can be understood by estimating the various contributions to the torque acting on a crystal (Sheikh et al. 2020), which leads to the conclusion that under a broad range of conditions, particles settle preferentially with their largest dimension oriented perpendicular to their direction of fall (Kramel 2017; Menon et al. 2017; Gustavsson et al. 2019). Gustavsson et al. (2019) undertook a complete study to describe the statistics of crystals orientation in turbulent flow by taking into account fluid inertia in the expressions of the force and torque acting on a spheroid (Cox 1965; Khayat and Cox 1989; Dabade et al. 2015). This led to a full description of the statistics of orientations in the overdamped regime, i.e., when particle inertia can be neglected (Gustavsson et al. 2019), also derived by Anand et al. (2020). A description of the statistics of orientation appropriate for a wide range of cloud conditions, consistent with measured orientation distributions, has been more recently derived (Gustavsson et al. 2021), extending the earlier work of Klett (1995).

In this work, we perform direct numerical simulations of homogeneous isotropic turbulent flows, and follow the motion of spheroids, using the set of equations described in Dabade et al. (2015); Sheikh et al. (2020), and recently used in a cloud microphysics context by Gustavsson et al. (2021). We vary the energy dissipation range over the realistic range $1\,\mathrm{cm^2/s^3} \le \varepsilon \le 250\,\mathrm{cm^2/s^3}$, as well as the aspect ratio of the crystals, keeping the diameter fixed and equal to $300\,\mu$m, and we determine the collision kernels for these cases. We show that collisions may result from several possible effects. One mechanism, originally proposed by Saffman and Turner (1956), is due to the fact that the erratic turbulent motions may bring particles together. The possibility of a broad distribution of orientation favors collisions due to the different settling velocities of particles. Finally, at high turbulence intensity, the particle inertia becomes important, and makes it possible for particles not following the flow to collide. This effect, denoted as the 'sling effect' (Falkovich et al. 2001; Falkovich and Pumir 2007) or alternatively as a manifestation of 'caustics' (Wilkinson and Mehlig 2005; Wilkinson et al. 2006), enhances the probability of collisions in the suspension.

The problem studied here is complex, with a large number of mechanisms and non-dimensional parameters at play. In this paper we focus on the effect of particle and fluid inertia on ice-crystal collisions, using a highly idealised model that does not take into account interactions, which may become important when the crystals are close: hydrodynamic interactions (Shaqfeh and Koch 1990), Coulomb interactions (Magnusson et al. 2021), and the breakdown of hydrodynamics (the fact that the discrete molecular nature of the gas becomes important) when the gap between the particles is of the order of the mean free path of the ambient air (Sundararajakumar and Koch 1996). The model describes how the crystals approach, but cannot predict collision outcomes. When counting collisions we use a simplified approach, the ghost-collision scheme (Wang et al. 1998; Gustavsson et al. 2008; Gustavsson and Mehlig 2016), which simply counts how frequently crystals approach each other, disregarding any change in boundary conditions e.g. due to fragmentation or coalescence.

Our work is organized as follows. The simplifying assumptions made to treat the problem, as well as the numerical methodology are presented in section. 2. In section 3 we show results of our numerical simulations for the orientation, settling velocity and collisions of the crystals. The collision statistics are then discussed in section 4. Section 5 finally contains our conclusions.

2. Problem setup

The way we set up the problem here closely follows Jucha et al. (2018); Naso et al. (2018).

Turbulent flow simulations. Although turbulence in clouds is affected by various parameters, particularly by the flow stratification, we simplify the problem by restricting ourselves to homogeneous isotropic turbulence. Our work is based on direct numerical simulations of the Navier-Stokes equations:

$$\partial_t \mathbf{u} + (\mathbf{u}\cdot\nabla)\mathbf{u} = -\frac{\nabla p}{\rho_f} + \nu\nabla^2\mathbf{u} + \mathbf{f}, \tag{1}$$

$$\nabla\cdot\mathbf{u} = 0, \tag{2}$$

where $\mathbf{u}$ is the velocity of the fluid, p its pressure, ρ_f and ν are the mass density and kinematic viscosity, respectively. We take the values of $\rho_f = 1.413\times10^{-3}\,\mathrm{g/cm^3}$, and $\nu = 0.1132\,\mathrm{cm^2/s}$.

We use a triply periodic box, of size $L = 8\times\pi\mathrm{cm} \approx 25\,\mathrm{cm}$ in each spatial direction. The number of grid points, N, or equivalently of Fourier modes in each direction is varied to maintain sufficient accuracy to allow us to reliably interpolate the velocity field and its derivatives at the particle positions, as necessary to solve the equations of motion for the particles. We insisted in our simulations that the largest wavenumber resolved, k_{max}, satisfies $\eta k_{max} \gtrsim 3$, where $\eta = (\nu^3/\varepsilon)^{1/4}$ is the size of the smallest eddies in the flow (η is known as the Kolmogorov scale). Further details about the code can be found in Jucha et al. (2018); Naso et al. (2018). We picked three values of ε, $\varepsilon \approx 1\,\mathrm{cm^2/s^3}$ (flow I, runs 1-3), $\varepsilon \approx 16\,\mathrm{cm^2/s^3}$ (flow II, runs 4-7) and $\varepsilon \approx 250\,\mathrm{cm^2/s^3}$ (flow III, runs 8-10), further details are given in Table 1.

Ice crystals: elementary simplifications. We focus here on small planar ice-crystals, whose shape we approximate as oblate spheroids. More precisely, we consider an ellipsoid of revolution, with a semi-major axis a and a semi-minor axis c, the aspect ratio $\beta = c/a$ being taken very small, $\beta = 0.005$, 0.01, 0.02 and 0.05. We added the smallest value, $\beta = 0.005$, compared to the set of values considered in Jucha et al. (2018), to better illustrate the interplay between different physical effects, as discussed in Section 4.

As the volume fraction of particles in clouds is very small, it is justified to ignore the feedback of the particles on the flow, and to use the one-way coupling approximation (Elgobashi 1994).

The motion of the crystals is obtained by solving Newton's equations in the inertial reference frame for the center of mass of the particle, $\mathbf{x}$, and for its velocity, $\mathbf{v}$, as well as for the orientation, $\hat{\mathbf{n}}$, defined as the unit vector parallel to the axis of symmetry of the spheroid, as illustrated in Fig. 1, and for its angular velocity, $\boldsymbol{\omega}$:

$$\frac{d\mathbf{x}}{dt} = \mathbf{v}\,, \quad m\frac{d\mathbf{v}}{dt} = \mathbf{f}_h + m\mathbf{g}, \tag{3}$$

where $\mathbf{f}_h$ is the hydrodynamic force acting on the particle, and

$$\frac{d\hat{\mathbf{n}}}{dt} = \boldsymbol{\omega}\times\hat{\mathbf{n}}\,, \quad m\frac{d}{dt}\left[\mathbb{I}(\hat{\mathbf{n}})\boldsymbol{\omega}\right] = \boldsymbol{\tau}_h, \tag{4}$$

where $\boldsymbol{\tau}_h$ is the hydrodynamic torque acting on it. In Eqs. (3) and (4), m denotes the mass of the particles, and $\mathbb{I}(\hat{\mathbf{n}})$ the moment of inertia tensor, whose expression is given in Appendix A. The modeling challenge consists in providing the correct expressions for the force $\mathbf{f}_h$ and for the torque $\boldsymbol{\tau}_h$ exerted by the fluid on the particles.

Our approach rests on the assumption that the particle Reynolds number $Re_p = a|\mathbf{u}-\mathbf{v}|/\nu$, based on the difference between the flow velocity $\mathbf{u}$ and the particle velocity $\mathbf{v}$, is small. Under this condition, it is often assumed that the hydrodynamic force and torque acting on the ice crystals can be derived in the Stokes limit, i.e. when all the nonlinear terms in the Navier-Stokes equations can be neglected (Kim and Karrila 1991; Jeffery 1922). In this approach, the effect of fluid inertia is therefore completely neglected (Siewert et al. 2014b; Jucha et al. 2018; Gavze and Khain 2022). When the carrying flow is turbulent, such an assumption leads to the qualitatively incorrect conclusion that particles tend to settle with their major axis oriented parallel to gravity (Siewert et al. 2014a; Gustavsson et al. 2017).

In fact, the Reynolds number happens to be of order unity in the realistic parameter regime considered here, see also Jucha et al. (2018). For these reasons, the first correction induced by fluid inertia must be accounted for in the expressions of $\mathbf{f}_h$ and $\boldsymbol{\tau}_h$, in a systematic expansion in powers of Re_p. Whereas the correction to the force has been known for some time (Brenner 1961; Khayat and Cox 1989), the expression for the torque in the small Re_p limit has been derived more recently (Dabade et al. 2015). The explicit forms of the force $\mathbf{f}_h$ and of the torque $\boldsymbol{\tau}_h$ including both the Stokes contribution and the first effect of fluid inertia are provided in Appendix A. They have been validated numerically by directly solving the Navier-Stokes equations around a spheroid (Jiang et al. 2021), and confronted to experimental measurements of cylindrical fibers settling in a viscous fluid (Cabrera et al. 2022). A systematic analysis of the resulting equations (Sheikh et al. 2020; Gustavsson et al. 2021) (see also Kramel (2017); Anand et al. (2020)) shows that when the settling velocity U_s is large compared to the velocity of the smallest eddies in the flows, $u_K = (\nu\varepsilon)^{1/4}$, then the torque induced by fluid inertia prevails over the Stokes torque, which can lead to a preferential orientation of the spheroids with their largest dimension perpendicular to gravity. We stress that the novel aspect of the present work compared to the study

TABLE 1. Properties of the three turbulent flows used in this study. We simulated homogeneous isotropic flows in triply periodic boxes of size $L = 8\pi\,\mathrm{cm} \approx 25\,\mathrm{cm}$, with a fixed viscosity $\nu = 0.1132\,\mathrm{cm^2/s}$, injecting a fixed amount of energy ε in the system. We took three different values of ε, resulting in three different flows, as listed in the table. The Taylor-scale Reynolds number Re_λ, the Kolmogorov time τ_K, the integral time T_L, and the *rms* velocity fluctuation u_{rms} are listed for the three flows. The resolution for each run is N^3.

Flow	I	II	III
ε ($\mathrm{cm^2/s^3}$)	0.976	15.62	246.4
Re_λ	55.8	94.6	151.2
τ_K (s)	0.341	0.085	0.021
T_L (s)	1.96	0.70	0.26
u_{rms} (cm/s)	2.18	5.72	14.4
N	384	768	1536

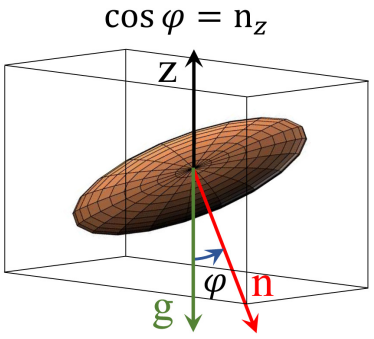

FIG. 1. Representation of a planar ice crystal by an oblate spheroid. The vector $\hat{\mathbf{n}}$ characterizing the orientation of the crystal is parallel to the axis of symmetry, and points downward. The angle φ is the angle between $\mathbf{g}$ and $\hat{\mathbf{n}}$.

of Jucha et al. (2018) comes from the use of force and torque expressions including the effect of fluid inertia. This modification plays a very significant role in predicting the distribution of orientations of the crystals, as documented by Gustavsson et al. (2021) (recall that considering the Stokes torque only led to a preferential orientation of the spheroids with their major axis aligned with gravity). We will show in Sec. 3 and discuss in Sec. 5 the effect of this correction on the crystal-crystal collisions.

The equations of motion of the particles, Eqs. (3,4), involve several important dimensional quantities (Gustavsson et al. 2021). The first one is τ_p, the characteristic time of the particle originating from the Stokes drag, and the second one is w_s, the typical settling velocity, which we take, following Jucha et al. (2018), to be respectively equal to:

$$\tau_p = \frac{2}{9}\frac{\rho_p}{\rho_f}\frac{\beta a^2}{\nu} \quad \text{and} \quad w_s = g\tau_p. \tag{5}$$

It is convenient to make the time τ_p and the velocity w_s dimensionless by dividing them respectively by τ_K and by the velocity across the smallest eddies in the flow, $u_K \equiv (\nu\varepsilon)^{1/4}$. This leads to the definitions of the Stokes number St and of the settling number Sv, which characterizes the settling velocity (Devenish et al. 2012; Wang and Maxey 1993; Grabowski and Vaillancourt 1999; Gustavsson et al. 2021), as:

$$\mathrm{St} = \frac{4\beta}{9}\frac{\rho_p}{\rho_f}\left(\frac{a}{\eta}\right)^2 \quad \text{and} \quad \mathrm{Sv} = \frac{4\beta}{9}\frac{\rho_p}{\rho_f}\frac{a^2 g}{(\nu^5\varepsilon)^{1/4}}, \tag{6}$$

where we recall that $\eta = (\nu^3/\varepsilon)^{1/4}$ is the Kolmogorov scale. Note that the quantities Sv and St, as defined by Eq. (6), differ by a factor 2 from the ones used in Gustavsson et al. (2021).

The approach used to solve the equations of motion for the crystals, Eq. (3,4), follows the method introduced by Siewert et al. (2014a) and by Jucha et al. (2018). Equation (3) has been integrated in time by using a second-order Heun scheme (two-stage Runge-Kutta method). The fluid velocity and velocity gradients at the particle location are estimated from grid values by a tricubic interpolation. Equation (4) for the angular velocity is integrated in time in the particle-fixed coordinate system (center of mass and principal axes) where the moment of inertia tensor is constant and diagonal. The spatial rotation between the inertial and the particle-fixed frame is conveniently handled by using quaternions and tracking the orientation of each particle. Let us note that an additional inertial term arises in the (transformed) equation due to the non-Galilean nature of the particle-fixed frame. Equation (4) was also integrated in time with a second-order Heun scheme. Consistent with the periodic boundary conditions used, we reinjected particles leaving the box through one of the sides to the opposite side. In all the runs considered in this work, the characteristic time taken by a particle to settle through the box is larger than $\gtrsim 2.5T_L$, where T_L is the large-eddy turnover time. Therefore, the flow has time to decorrelate between two passages of the particles.

Collision detection. Numerically, we determine the geometric collision rate (Wang et al. 2005; Ayala et al. 2008b; Grabowski and Wang 2013). This approximation neglects the hydrodynamic interactions, as well as any interaction between particles as they approach each other (Pruppacher and Klett 1997; Batchelor and Green 1972; Chun et al. 2005). Furthermore, we simply detect, from a large set of numerical trajectories of ellipsoids, the instants when two particles get into contact ("collide") with each other, while keeping the two colliding particles thereafter without any modification. The errors induced by this approximation, known as the "ghost-collision" approximation (Wang et al. 1998; Gustavsson et al. 2008; Gustavsson and Mehlig 2016), do not exceed ~ 15% in the case of spherical particles in a turbulent flow (Voßkuhle et al. 2013).

To determine when a collision occurs, we implemented the algorithm developed by Choi et al. (2009) to detect when two ellipsoids, moving in three dimensions, touch each other. The algorithm has been used successfully to detect collisions of settling ellipsoids in a turbulent flow (Siewert et al. 2014b; Jucha et al. 2018).

In practice, we simulated a million trajectories for each type of particle, for a time of $\geq 50T_L$ for flow I, $\geq 30T_L$ for flow II and $\geq 20T_L$ for flow III. Note that we waited before recording any property for at least $50\tau_\eta$, so the particles could reach a statistically steady state. The data shown in the following sections correspond to $\gtrsim 25{,}000$ collisions. We also checked the statistical significance of the numbers discussed below by dividing the total run into four or five identical sub-runs, and determining the number of collisions for each of these sub-runs. These comparisons

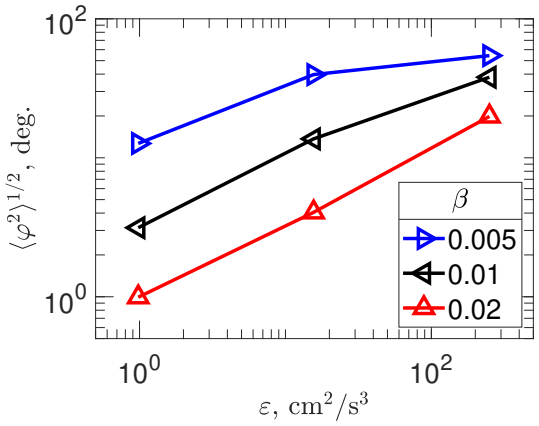

FIG. 2. Statistics of orientation: fluctuations of the angle of the settling spheroids with respect to the equilibrium position ($\varphi = 0$ in still fluid). For each point, the statistical uncertainty has been evaluated by calculating the deviations between four subsets of the total data. The resulting deviations are $\lesssim 5\%$ in most cases; they are $\sim 7\%$ and $\sim 10\%$ for the ($\varepsilon \approx 1, \beta = 0.005$) and ($\varepsilon \approx 250, \beta = 0.02$) cases, respectively.

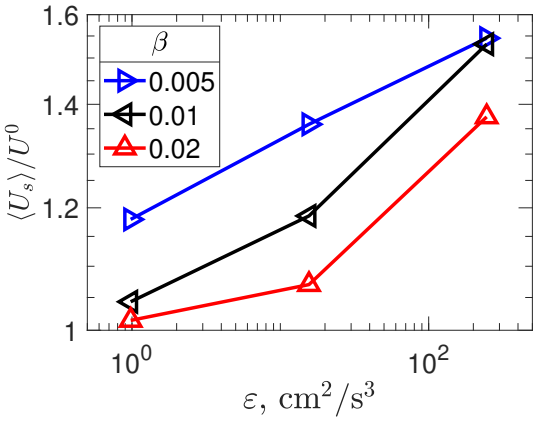

FIG. 3. Dependence of the averaged settling velocity of crystals as a function of β and ε. The three curves show the ratio between the averaged settling velocity U_s and the settling velocity of the same crystals in still fluid, U^0, as a function of the energy dissipation. Each curve corresponds to a value of β ($\beta = 0.005$: rightwards pointing triangles; $\beta = 0.01$: leftwards pointing triangles, and $\beta = 0.02$: upwards pointing triangles). The settling velocity increases with the intensity of turbulence. The statistical uncertainty has been evaluated using the same method as in Fig. 2. The deviations are always $\lesssim 3\%$, except for the ($\varepsilon \approx 1, \beta = 0.005$) case, for which it is $\sim 7\%$.

convinced us that the values of the collision kernel K shown below are accurate to within a few percents.

3. Results

In this Section, we discuss the results of our model simulations. A summary of the runs, on which the following discussion is based, can be found in Table B1, see Appendix B.

a. Orientation and settling velocity of the crystals

The orientation of the settling crystals is a crucial aspect for the physical effects leading to collision between crystals, in addition to its importance to explain the reflection of light by crystals in clouds (Klett 1995; Bréon and Dubrulle 2004; Yang et al. 2015). We recall that in the absence of any flow, oblate spheroids settle with their major axis oriented perpendicular to gravity. In the case of plate-like ice crystals, the unit vector parallel to the axis of symmetry of particle, $\hat{\mathbf{n}}$, is therefore parallel to $\hat{\mathbf{g}}$, the vertical direction, parallel to the gravity $\mathbf{g} \equiv |\mathbf{g}|\,\hat{\mathbf{g}}$. We pick the vector $\hat{\mathbf{n}}$ to point downward, so that $\hat{\mathbf{n}} \cdot \hat{\mathbf{g}} \geq 0$, and we denote the angle between $\hat{\mathbf{n}}$ and $\hat{\mathbf{g}}$ as φ, as illustrated in Fig. 1. Numerically, we recorded the fluctuations of φ of the simulated particles settling through the flow.

Figure 2 shows the *rms* of the angle fluctuations, $\langle\varphi^2\rangle^{1/2}$, for all our runs except run 7 (flow II and $\beta = 0.05$). This figure shows the dependence of $\langle\varphi^2\rangle^{1/2}$ as a function of the turbulence intensity ε, for the three values of β: $\beta = 0.005$ (rightwards pointing triangle), $\beta = 0.01$ (leftwards pointing triangle) and $\beta = 0.02$ (upwards pointing triangle). The behavior shown in Fig. 2 follows the predictions of our earlier studies (Gustavsson et al. 2021). Specifically, we find that the orientation distribution of the crystals is very narrowly peaked around $\varphi = 0$ at low values of ε, and becomes broader as the turbulence intensity increases. Figure 2 also shows that the distribution of particle orientation is more peaked when β is large, and becomes broader when β decreases. In quantitative terms, we observe that the fluctuation of the particle orientation does not exceed 4° for $\varepsilon \approx 1\,\mathrm{cm}^2/\mathrm{s}^3$ and $\beta \geq 0.01$, and for $\varepsilon \approx 16\,\mathrm{cm}^2/\mathrm{s}^3$ and $\beta \geq 0.02$, see Table B1.

Settling velocity. We begin by stressing that, as shown by Gustavsson et al. (2021), the model used here predicts settling velocities in still air in good agreement with those observed experimentally (Pruppacher and Klett 1997). The first effect of the orientation fluctuations is to affect the settling velocity of the crystals. This is illustrated in Fig. 3, which shows the averaged settling velocity, $U_s = -v_z$, where v_z is the vertical component of velocity (see Fig. 1). In Fig. 3, U_s is normalized by the velocity of particles settling in still fluid, U^0. The ratios are very close to 1 at low values of ε, and gradually increase with ε. A first explanation for this is provided by the finding summarized above, that the orientation distribution broadens due to the increase of the turbulence intensity. In fact, the largest drag in the direction of gravity is obtained when $\varphi = 0$; so increasing φ leads to a smaller drag, and therefore to a larger settling velocity. A larger *rms* of the orientation fluctuation therefore increases the settling velocity U_s,

compared to the reference value U^0 in the absence of any fluid motion. The effect of turbulence on the settling of particles has been widely investigated for spherical objects (Good et al. 2014; Ireland et al. 2016; Rosa et al. 2016): turbulence most often increases their settling velocity, as observed herein for spheroidal particles, and more rarely decreases it. Several physical mechanisms were proposed to explain these results: the preferential sweeping (Maxey 1987), according to which heavy particles should sample preferentially downflow regions, is expected to increase the settling, whereas the loitering effect (falling particles spend more time in the regions with upward flow) (Nielsen 1993) and vortex trapping should decrease the settling velocity.

The increase in the settling velocity when the orientation of the crystal differs from $\varphi = 0$ is further illustrated in Fig. 4, which shows the average of the settling velocity of crystals conditioned on the cosine of the angle φ, or equivalently, on the z-component of the vector $\hat{\mathbf{n}}$ aligned with the axis of symmetry of the spheroid, see Fig.1. The orientation $\varphi = 0$ corresponds here to $n_z = 1$. The conditional averages shown in Fig. 4 correspond to the thinnest crystals, with the value of $\beta = 0.005$, at the different values of ε. For the three turbulence intensities, the numerical results reveal a clear increase of the settling velocity when n_z decreases towards 0. For the lowest turbulence intensity, the settling velocity at $n_z \approx 0$, corresponding to a particle oriented with its major axis parallel to gravity, is roughly equal to 3/2 times the velocity of the particle settling with $n_z = 1$ (major axis perpendicular to gravity), which corresponds to the ratio between the drag of the particles settling with the two orientations in a quiescent fluid. As seen in a previous study, where the effect of fluid inertia on the dynamics of crystals was (incorrectly) neglected (Siewert et al. 2014b; Jucha et al. 2018), the systematic difference of the settling velocity on the crystal orientation plays an important role and tends to enhance collisions. Interestingly, we notice that the value of the settling velocity conditioned on $n_z \approx 1$ is lower than the expected value in a quiescent fluid for the highest turbulence intensity. This result suggests that ice crystals with their major axis oriented perpendicular to gravity may be more sensitive to the loitering effect and vortex trapping, and/or less sensitive to preferential sweeping.

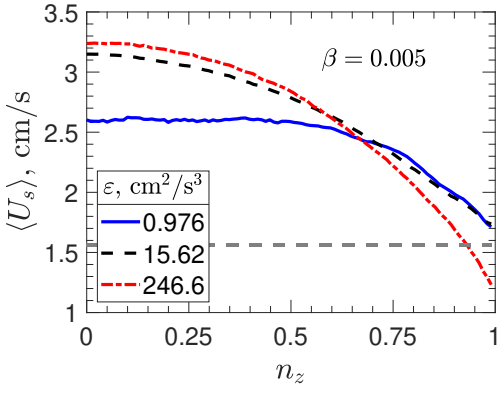

FIG. 4. Averaged settling velocity conditioned on the orientation of the crystal, represented by n_z, the vertical component of $\hat{\boldsymbol{n}}$. The three curves correspond to $\beta = 0.005$ and to the three values of ε, as indicated by the legend. The horizontal gray dot-dashed line shows the settling velocity in a fluid at rest, with $n_z = 1$, which is the only steady and stable regime in this case.

b. *The collision kernel*

In a dilute solution of volume V, containing N particles, the average number of collisions, N_c, occurring over a duration T, is proportional to T, to the inverse of the volume, V^{-1}, and to N^2, and can therefore be written as (Voßkuhle et al. 2013; Jucha et al. 2018):

$$N_c = \frac{1}{2} K \times \frac{N^2}{V} \times T \tag{7}$$

where K is the collision kernel. The dimension of K is a volume divided by a time.

Figure 5 shows the collision kernels K determined numerically for our model system. Figure 5(a) shows the dependence of K on ε, at the values $\beta = 0.005$, 0.01 and 0.02. Our results are consistent with the expectation that in-

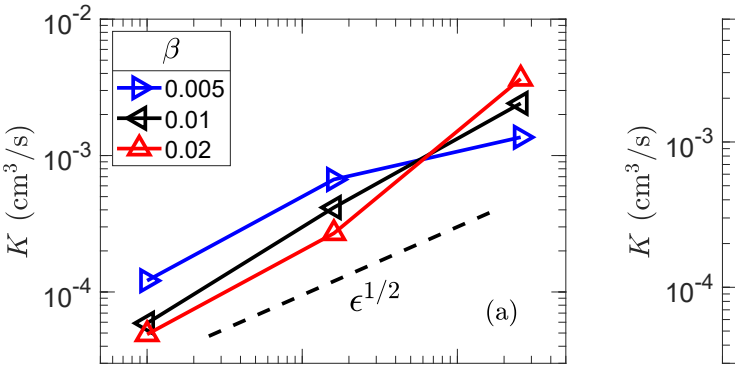

FIG. 5. Dependence of the collision kernel on: (a) the energy dissipation for $\beta = 0.005$ (right-pointing triangles), 0.01 (left-pointing triangles) and 0.02 (upper-pointing triangles), and on (b): β at $\varepsilon \approx 1\,\mathrm{cm}^2/\mathrm{s}^3$ (+ symbols), $\varepsilon \approx 16\,\mathrm{cm}^2/\mathrm{s}^3$ (diamond symbols) and $\varepsilon \approx 250\,\mathrm{cm}^2/\mathrm{s}^3$ (square symbols). The statistical uncertainty has been evaluated using the same method as in Fig. 2. The deviations are always between 2 and 7%, except for the ($\varepsilon \approx 250, \beta = 0.02$) case, for which it is ~ 9%.

creasing the turbulence intensity enhances the probability of collision. As a reference, we indicate as a dashed line the $\varepsilon^{1/2}$ dependence, expected when collisions are due to the velocity gradients bringing particles together (Saffman and Turner 1956; Jucha et al. 2018). Whereas the dependence of K on ε is qualitatively close to this expectation when ε varies from $\approx 1\,\mathrm{cm}^2/\mathrm{s}^3$ (flow I) to $\approx 16\,\mathrm{cm}^2/\mathrm{s}^3$ (flow II), the evolution at higher values of ε shows a strong deviation from this behavior. The collision rate K for the thickest particles, $\beta = 0.02$, which was smaller for $\varepsilon \leq 16\,\mathrm{cm}^2/\mathrm{s}^3$, grows far more rapidly than $\varepsilon^{1/2}$. On the other hand, for the thinnest crystals, with $\beta = 0.005$, the value of K, which was the largest at $\varepsilon \leq 16\,\mathrm{cm}^2/\mathrm{s}^3$, grows slower than $\varepsilon^{1/2}$ between $\varepsilon \approx 16\,\mathrm{cm}^2/\mathrm{s}^3$ and $\varepsilon \approx 256\,\mathrm{cm}^2/\mathrm{s}^3$. Remarkably, whereas the collision rate decreases at increasing β for $\varepsilon \lesssim 16\,\mathrm{cm}^2/\mathrm{s}^3$, it increases at the largest value of ε simulated, as shown on Fig. 5(b). This complex dependence on the parameters of the problem can only be interpreted as the result of a competition between several different physical mechanisms in the dynamics of collisions. The following section is devoted to a closer analysis of these mechanisms.

4. Discussion

a. Collision mechanisms

The original Saffman-Turner theory (Saffman and Turner 1956), valid for particles following exactly the flow, provides a convenient starting point to discuss the collision mechanisms at play in the present problem. We recall that the physics is based on expressing the collision kernel K in a turbulent suspension of spheres, of radius $\overline{a}$, as a flux of particles through a sphere centered at the position of a given particle in the suspension, of radius $2\overline{a}$, the particles being brought together by the velocity gradient. Considering two colliding particles at positions $\mathbf{x}_1$ and $\mathbf{x}_2$, with $\hat{\mathbf{r}}$ defined as $\hat{\mathbf{r}} = (\mathbf{x}_2 - \mathbf{x}_1)/||\mathbf{x}_2 - \mathbf{x}_1||$, and moving with velocity $\mathbf{v}_1$ and $\mathbf{v}_2$, the relative velocity of the particles is then expected to scale as:

$$\Delta v_r \equiv (\mathbf{v}_2 - \mathbf{v}_1) \cdot \hat{\mathbf{r}} \sim \overline{a}/\tau_K. \tag{8}$$

The quantity Δv_r (see Fig. 6(d)) is the relative velocity between the centers of mass of two colliding particles. A negative value of Δv_r means that these centers of mass are approaching each other, whereas a positive value reflects the fact that they are moving away from each other. For spherical particles, a collision is only possible when $\Delta v_r < 0$, but the rotational motion of spheroidal objects allows them to collide with $\Delta v_r > 0$.

We postulate here that the rotational degrees of freedom, i.e. the fluctuations in the orientation of the crystals, will not affect the estimate provided by Eq. (8) for spheres. In this spirit, Fig. 6(a-c) show the distribution of the relative velocity Δv_r between colliding crystals. To make Δv_r dimensionless, we divide it by the characteristic velocity induced by the velocity gradients when two spheroids come close to each other. We estimate this velocity as the ratio a/τ_K, where we recall that a is the semi-major axis of the spheroid. The three different panels present our results at three different values of ε, in increasing order of ε from (a) to (c).

Remarkably, at the lowest turbulence intensity, $\varepsilon \approx 1\,\mathrm{cm}^2/\mathrm{s}^3$, the PDFs of Δv_r almost perfectly superpose for $\beta = 0.01$ (dashed black line) and $\beta = 0.02$ (dashed-dotted red line). In fact, the center of the PDF of Δv_r at $\beta = 0.005$ (continuous blue line) is also very similar to those at higher values of β. However, a difference can be seen by the appearance of a broad tail biased towards very negative values of $\Delta v_r \tau_K / a$, with a probability of $\approx 2\ 10^{-3}$ times the maximum probability. To understand the origin of this broad tail for $\beta = 0.005$, it is useful to recall that at this low turbulence intensity and for $\beta = 0.01$ and $\beta = 0.02$, the *rms* of the orientation fluctuations are extremely small (of the order of $\sim 3°$ or less); they are slightly larger for $\beta = 0.005$ ($\sim 13°$). This increased value of $\langle \varphi^2 \rangle^{1/2}$ implies a distribution of orientation that is not as sharply peaked around $\varphi \approx 0$. As shown in Fig.4, the settling velocity of crystals with a sufficiently small value of $n_z \equiv |\cos(\varphi)|$ (say for $n_z \lesssim 0.6$) can exceed the averaged settling velocity by approximately $1\,\mathrm{cm/s}$. This corresponds to $\Delta v_r \tau_K / a \approx 22$, which is close to the horizontal extent of the broad tail towards negative values of Δv_r. This horizontal extent of the blue curve in Fig. 6(a) is therefore close to the excess of settling velocity of the fastest ice crystals (those oriented with their major axis close to vertical) with respect to the averaged settling velocity. As a consequence, we interpret the broad negative tails of the PDFs as a signature of the differential settling effect: faster ice crystals, oriented predominantly "vertically", catch up with slower ones underneath, oriented "horizontally".

Further evidence for the role of differential settling can be obtained by comparing the collision kernel K to its value K^0 in the same flow but turning off gravity (see the two last columns of Table B1). Whereas the values of K and K^0 are very close when $\beta \geq 0.01$, the ratio between K and K^0 becomes ≈ 3 for $\beta = 0.005$, an effect that we attribute to the differential settling between crystals. We note that the values of K^0 are very close to the values of K^0 found in Jucha et al. (2018), implying that the dynamics of orientation does not matter much to estimate the collision kernel if gravity was absent. On the contrary, in the realistic system, the much stronger alignment of the crystals with the direction of gravity in the present study leads to a strong reduction of differential settling, resulting in much lower values of K compared to Jucha et al. (2018).

The structure of the PDFs of Δv_r at the intermediate value of $\varepsilon \approx 16\,\mathrm{cm}^2/\mathrm{s}^3$, shown in Fig. 6(b), points to an increased importance of the differential settling between crystals, compared to the situation at $\varepsilon \approx 1\,\mathrm{cm}^2/\mathrm{s}^3$. Once

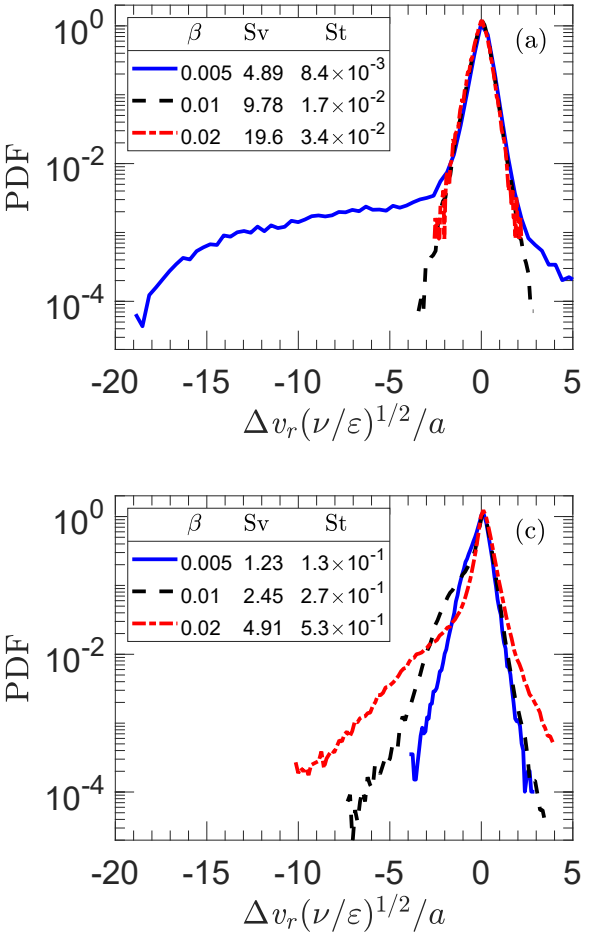

FIG. 6. (a-c) Probability density function of the velocity difference between two colliding particles, defined by Eq. (8), and made dimensionless by dividing by a/τ_K. Increasing turbulence intensity from (a) to (c). The cores of the distributions closely superpose with each other. The broad tails reflect the effect of differential settling at low ($\varepsilon \approx 1\,\mathrm{cm}^2/\mathrm{s}^3$, top) or at intermediate ($\varepsilon \approx 16\,\mathrm{cm}^2/\mathrm{s}^3$, middle) turbulence intensity, or the sling effect, at the highest turbulence intensity ($\varepsilon \approx 250\,\mathrm{cm}^2/\mathrm{s}^3$, bottom). (d) Illustration of the definition of the relative velocity Δv_r [Eq. (8)].

again, the cores of the distributions for the three different values of β superpose very well, which indicates that the vast majority of collisions between crystals at this intermediate turbulence intensity are due to particles being brought together by the action of the velocity gradients. In the cases $\beta = 0.005$ (full blue line), and $\beta = 0.01$ (dashed black line), one observes broader tails corresponding to very negative values of Δv_r. Compared to the lower turbulence intensity, $\varepsilon \approx 1\,\mathrm{cm}^2/\mathrm{s}^3$, the value of the probability where the broad tail develops at $\beta = 0.005$ is much higher when $\varepsilon \approx 16\,\mathrm{cm}^2/\mathrm{s}^3$. This reflects the much broader distribution of crystal orientation, and in particular the larger probability of having particles with $n_z < 0.6$. A quantitative comparison shows that the broader tails observed for $\beta = 0.005$ and $\beta = 0.01$ in the distributions of $\Delta v_r \times \tau_K/a$ can be attributed to the fluctuations of orientation, with $n_z \lesssim 0.6$. In comparison, for $\beta = 0.02$, the distribution of $\Delta v_r \times \tau_K/a$ remains peaked around the center, without any visible deviation. The role of differential settling as a collision mechanism, clearly demonstrated for $\beta = 0.005$ and $\beta = 0.01$ by Fig. 6(b), can be further evidenced by comparing the collision kernel values in the presence and in the absence of gravity (Table B1): $K > K^0$ for $\beta \leq 0.01$, whereas $K \lesssim K^0$ for $\beta \geq 0.02$.

Before discussing the last panel of Fig. 6, it is useful to notice that the particle Stokes numbers for $\varepsilon \lesssim 16\,\mathrm{cm}^2/\mathrm{s}^3$ are small. The largest value, for $\beta = 0.02$ and $\varepsilon \approx 16\,\mathrm{cm}^2/\mathrm{s}^3$ is $\mathrm{St} \approx 0.14$. These values, which are multiplied by ≈ 4 at $\varepsilon \approx 250\,\mathrm{cm}^2/\mathrm{s}^3$, become 0.13 for $\beta = 0.005$, 0.27 for $\beta = 0.01$ and 0.54 for $\beta = 0.02$. In this context, we recall that when the Stokes number is no longer small (~ 0.3), the effect of particle inertia becomes prevalent, and as a consequence particles do not follow very closely the fluid velocity. This is the origin of the 'sling effect' (Falkovich et al. 2002; Falkovich and Pumir 2007) (see also Wilkinson and Mehlig (2005); Wilkinson et al. (2006)), caused by particles colliding at a velocity Δv_r much larger than predicted by Eq. (8), therefore greatly enhancing the collision rates (Gustavsson and Mehlig 2011; Voßkuhle et al. 2014; Pumir and Wilkinson 2016). Consistent with the notion that the relative velocity between colliding particles can be greatly enhanced by the 'sling effect', the third panel of Fig. 6, corresponding to $\varepsilon \approx 250\,\mathrm{cm}^2/\mathrm{s}^3$, reveals in fact a broad widening of the tails of the distribution of $\Delta v_r \times \tau_K/a$ for $\beta = 0.01$ and $\beta = 0.02$.

At the smallest value $\beta = 0.005$, the PDF of $\Delta v_r \times \tau_K/a$ appears as very similar to that obtained at lower turbulence intensity, in the absence of any marked effect of differential settling. In fact, the PDF of $\Delta v_r \tau_K/a$ superposes very well with those at $\varepsilon \approx 1\,\mathrm{cm}^2/\mathrm{s}^3$ and $\beta \geq 0.01$, and $\varepsilon \approx 16\,\mathrm{cm}^2/\mathrm{s}^3$ and $\beta = 0.02$. The differential settling effect induces a very slight shoulder in the distribution at $\beta = 0.005$ and $\varepsilon \approx 250\,\mathrm{cm}^2/\mathrm{s}^3$, which is to be expected since the contribution to $\Delta v_r \tau_K/a$ due to differential settling in this configuration is of order ~ 3, and does not appear as major contribution to the distribution of relative velocity.

In comparison, the broadening of the distribution of $\Delta v_r \tau_K/a$ at $\beta = 0.01$ and $\beta = 0.02$ exceeds by far what is expected from differential settling. In fact, the values of $U_s \tau_K/a$ are of the order of $5-6$, much smaller than the extent of the PDFs shown in Fig. 6(c). This leads us to the conclusion that the mechanism leading to enhancement of the collision rate, much stronger than differential settling, is related to the generation of very large velocity differences, which we attribute to the above-mentioned effects

of particle inertia (Falkovich et al. 2001; Wilkinson and Mehlig 2005).

Further evidence for the importance of such inertial effects can be obtained by studying the collision rate in the absence of gravity. The numerical results presented in Appendix C indicate that the collision rate for $g = 0$, K^0, scales as $\sim \varepsilon^{1/2}$ for all cases where the Stokes number St < 0.1. This scaling corresponds to the Saffman-Turner prediction, valid for weakly inertial particles. We recall that in the related problem of colliding spherical particles, inertial effects are found to be immaterial for St $\lesssim 0.1$ (Voßkuhle et al. 2014). Consistent with the results of Jucha et al. (2018), obtained from a model that ignores the fluid inertia, the present results indicate that the same criterion applies in the case of spheroids. Namely, as shown in Table B1, inertia is found to be weak (St ≤ 0.1) in all simulations with $\varepsilon \approx 1\,\mathrm{cm}^2/\mathrm{s}^3$, and in those with $\varepsilon \leq 16\,\mathrm{cm}^2/\mathrm{s}^3$ for $\beta \leq 0.01$. At $\beta = 0.02$ and $\varepsilon \approx 16\,\mathrm{cm}^2\mathrm{s}^3$, deviations from the $\varepsilon^{1/2}$ scaling are visible, see Fig. C1. The deviation from the $\sim \varepsilon^{1/2}$ is very clear at $\varepsilon = 256\,\mathrm{cm}^2/\mathrm{s}^3$ and $\beta \geq 0.01$, for which the Stokes numbers vary between St = 0.134 ($\beta = 0.005$) and 0.536 ($\beta = 0.02$). We observe that at $\varepsilon \approx 250\,\mathrm{cm}^2/\mathrm{s}^3$, the values of K are close to the values of K^0 in the absence of gravity, providing further evidence that differential settling does not play a major role when the turbulence intensity is large. We stress that the discussion about the role of inertial effects in determining the collision rate in the absence of gravity is qualitatively completely consistent with the observations of Fig. 6.

It is worth stressing the role of fluid inertia in the problem. Comparing the results in Siewert et al. (2014b); Jucha et al. (2018) with those of the present study clearly shows the role of fluid inertia. These effects, which are particularly significant in our study for $\varepsilon \lesssim 16\,\mathrm{cm}^2/\mathrm{s}^3$, can be traced back to the properties of preferential orientation. Taking into account the effect of fluid inertia on the orientation dynamics drastically changes the nature of the orientation bias. In particular, the distributions of orientation are extremely peaked at the smallest value of the energy dissipation, $\varepsilon \approx 1\,\mathrm{cm}^2/\mathrm{s}^3$. As a result, the strong dispersion of settling velocity observed in Jucha et al. (2018) almost completely disappears when taking into account the effect of fluid inertia, except for the lightest crystals considered here ($\beta = 0.005$).

b. Representation of the different regimes in the parameter space.

The approach proposed by Gustavsson et al. (2021) predicts a parametrization of the distribution of orientation, in particular of the variance of the angle φ, as a function of two parameters, namely the Stokes number, St, and the settling number, Sv, defined by Eq. (6). In this subsection, we compare the prediction of that model with our own results, and discuss the implications for the various collision mechanisms introduced in Subsection 4a.

We begin by noticing that the parametrization in Gustavsson et al. (2021) actually involves the ratios $\mathrm{St}/A_\perp$ and and $\mathrm{Sv}/A_\perp$, where $A_\perp$ is one of the quantities defining the translational resistance tensor, defined in Appendix A. This coefficient $A_\perp$ is essentially constant for the very small values of β considered here. Quantitatively, the agreement between the fluctuations of orientation calculated in our simulations, and the predictions of the model used in Gustavsson et al. (2021), is generally quite good, see Table B1.

In the spirit of Figs. 3 and 5 of Gustavsson et al. (2021), Fig. 7 shows the variance of the orientation fluctuations, $\langle\varphi^2\rangle$, as a function of St and Sv. The figure also shows the points corresponding to the particles considered in the present work, color coded to stress the collisional mechanism involved for the corresponding runs, as discussed in Section 4a. The red points correspond to the purely Saffman-Turner mechanism. This collisional mechanism dominates when the angle fluctuations $\langle\varphi^2\rangle$ are very weak, for $\langle\varphi^2\rangle \lesssim 10^{-2}$, and when St is low enough (St $\lesssim 0.1$). The points for which the dominant collisional mechanism is provided by differential settling are marked in green. As the difference in the settling velocity is ultimately related to fluctuations in the orientation between crystals, this effect is only possible when the fluctuations of the angle φ are large enough. Judging from our numerical results, this occurs when $\langle\varphi^2\rangle \gtrsim 10^{-2}$ (this value corresponds to an r.m.s fluctuation of slightly less than 6°). The case $\beta = 0.005$ and $\varepsilon \approx 246\,\mathrm{cm}^2/\mathrm{s}^3$, shown by the full curve in Fig. 6(c), provides an example where the velocity differences due to differential settling were effectively immaterial, compared to $\sim a(\varepsilon/\nu)^{1/2}$, the typical velocity differences due to turbulence. The critical value of Sv below which differential settling does not lead to appreciable velocity differences with respect to the typical velocity differences induced by turbulence can be estimated by comparing the difference in the settling velocity, and the fluctuations of the relative velocities of the colliding crystals, shown in Fig. 6. Judging from this Figure, we estimate the value of Sv where the effect of differential settling becomes immaterial to Sv $\lesssim 1.5$. This transition region (like the two other ones) is indicated by a gray rectangle. For Sv < 1.5, we expect the Saffman-Turner mechanism to prevail.

Last, the crystals for which the dominant collisional mechanism is due to inertial effects are indicated in blue, and all correspond to Stokes number St $\gtrsim 0.1 - 0.2$. We have also added the point corresponding to $\beta = 0.05$ and $\varepsilon \approx 16\,\mathrm{cm}^2/\mathrm{s}^3$ (run 7 in Table B1), which appears as the point with the highest value of Sv. For the corresponding crystals, the Stokes number is St = 0.338, and the dominant collision mechanism is due to inertia.

We notice that two of the crystals considered have a Stokes

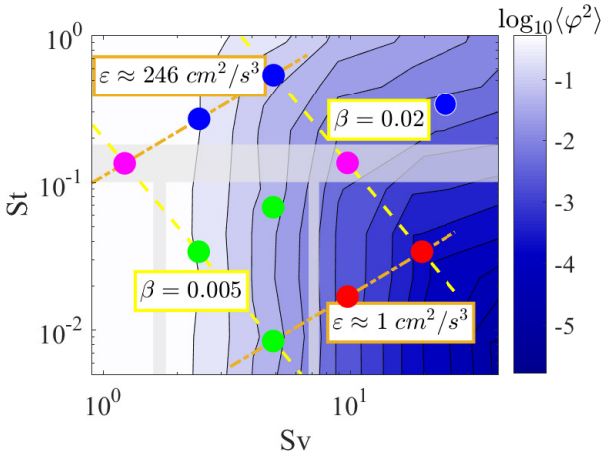

FIG. 7. Summary of the various regimes as a function of the two main parameters of the problem, namely the settling number, Sv (horizontal) and the Stokes number, St (vertical). The yellow dashed lines indicate the constant β-lines, and the orange dashed-dotted lines the constant ε-lines. The color code on the right corresponds to the fluctuations of the angle of orientation as a function of (Sv, St), as discussed in Gustavsson et al. (2021). The points used in the simulation are color coded according to the prevalent physical effect determining the collision: the dominant collision mechanisms is the Saffman-Turner mechanism (red points), the differential settling (green points), and the sling effect (blue points). The two magenta points correspond to transition regimes between several dominant collision mechanisms, which occur in the domains of parameters in transparent gray.

number St ≈ 0.13, right in the transition region when inertial effects become dominant. The two corresponding points have been marked by a magenta dot.

5. Conclusion

We have estimated numerically the rate of collisions between identical plate-like ice crystals in a turbulent flow. Our model involves a number of approximations, and is comparable with the study of Jucha et al. (2018) with the major difference that we considered here the effect of fluid inertia. Earlier studies had demonstrated the crucial role of this physical effect in the dynamics of orientation of crystals settling in a turbulent flow, leading to the tendency for crystals to settle with their maximal dimension oriented perpendicular to gravity (Lopez and Guazzelli 2017; Gustavsson et al. 2019; Sheikh et al. 2020; Gustavsson et al. 2021), contrary to what was observed in Siewert et al. (2014a); Gustavsson et al. (2017); Jucha et al. (2018).

Our numerical results concerning the collision statistics can be interpreted in terms of three main physical effects. The first one, as understood by Saffman and Turner (1956), is due to the effects of velocity gradients, which can bring particles together. At very large turbulence intensity, when the particle response time is larger than the characteristic times of the smallest eddies, the Kolmogorov time, particles do not exactly follow the flow, and can be "slung" out of eddies. The resulting sling effect tends to strongly increase the collision kernel of colliding particles. At low turbulence intensity, differential settling between particles of different orientations had been suggested to play a dominant role in studies that were not taking into account fluid inertia in the crystal dynamics (Siewert et al. 2014b; Jucha et al. 2018).

Remarkably, Fig. 7 suggests that the physical effects involved can be described by two parameters, St and Sv. This allows us to predict the main physical effects involved in the collision process in terms of these two parameters only. For this reason, we expect that the results of the present study can be expanded to describe plate-like crystals of various sizes (a and $\beta \ll 1$), over a broad distribution of turbulence intensity, provided the main hypotheses of the model are satisfied (size of the crystals a smaller than the Kolmogorov scale, and small enough particle Reynolds number). On the other hand, our results leave open the question of the collision rate between objects with a very different shape, such as elongated crystals, describable in terms of prolate ellipsoids.

As demonstrated here, the three mechanisms play a role in determining the collision kernel when using the more realistic model of crystal dynamics. The main difference with earlier studies not taking into account the fluid inertia comes from the very different role of differential settling in the dynamics leading to collisions. At weak turbulence intensities, the collision rates observed in Jucha et al. (2018) were larger by approximately a factor of 10 compared to the collision rates observed here. This is due to the very peaked distribution of orientation dynamics at large values of Sv, which effectively reduces the dispersion of orientation, and therefore of settling velocity, as soon as the settling number is $\gtrsim 5-10$. Using the definition of Sv, Eq. (6), and the values reported in Appendix B, we deduce that differential settling plays a role for $\varepsilon \gtrsim \beta^4 \times 1.6\ 10^8\,\mathrm{cm}^2/\mathrm{s}^3$.

The very strong bias in the orientation of crystals settling in turbulent flows is likely to also strongly affect the riming process, whereby small ice crystals collide in mixed-phase clouds with small droplets (Naso et al. 2018; Jost et al. 2019). Further studies devoted to this problem will be reported separately.

As mentioned in the Introduction, our model is highly idealised. In particular, it disregards crystal-crystal interactions that may become important at small separations, and does not model collision outcomes. Nevertheless, we expect that the model describes at least qualitatively how particle and fluid inertia change the way in which the crystals approach (and collide). In the future we intend to test the relevance of the ghost collision approach and to formulate a more detailed collision model that can reliably predict collision outcomes. Developing such an approach, which

is a necessary step to determine in quantitative terms the influence of the approximations used in the present work, is beyond the scope of this paper.

Acknowledgments. BM thanks Fabien Candelier for discussions regarding the inertial torque. MZS, AP and AN acknowledge support from the IDEXLYON project (Contract ANR-16-IDEX-0005) under University of Lyon auspices. MZS's PhD thesis was supported by a grant from the Higher Education Commission Pakistan. KG and BM were supported by the grant *Bottlenecks for particle growth in turbulent aerosols* from the Knut and Alice Wallenberg Foundation, Dnr. KAW 2014.0048, and in part by VR grant no. 2017-3865 and Formas grant no. 2014-585. Computational resources were provided by PSMN, C3SE and SNIC.

Data availability statement. The dataset on which this paper is based is too large to be retained or publicly archived with available resources. Documentation and methods used to support this study are available on request to the authors.

APPENDIX A

Equations of motion

We provide here explicit expressions for the force, $\mathbf{f}_h$, and for the torque, $\boldsymbol{\tau}_h$, acting on an oblate spheroid of semi-major axis a, semi-major axis c and aspect ratio $\beta = c/a < 1$.

As explained in the text, we express $\mathbf{f}_h$ and $\boldsymbol{\tau}_h$ as the sum of the force and torque, $\mathbf{f}_h^{(0)}$ and $\boldsymbol{\tau}_h^{(0)}$, obtained in the Stokes limit, by neglecting all the nonlinear terms in the Navier-Stokes equations Eq. (1) and valid when the particle Reynolds number Re_p is $\ll 1$, plus a correction induced by taking into account the fluid inertia in a perturbative expansion in powers of Re_p, $\mathbf{f}_h^{(1)}$ and $\boldsymbol{\tau}_h^{(1)}$.

a. Force and torque in the Stokes limit

The expression for the force $\mathbf{f}_h^{(0)}$ reads:

$$\boldsymbol{f}^{(0)} = 6\pi a\mu\mathbb{A}\big(\boldsymbol{u}-\boldsymbol{v}\big)\,, \tag{A1}$$

where $\mu = \rho_f \nu$ is the dynamic viscosity of the fluid, $\mathbb{A}$ is the resistance tensor, and $\boldsymbol{u}$ is the fluid velocity at the particle location. For a spheroid, the expression of the resistance tensor is known exactly, see e.g. Kim and Karrila (1991), and is recalled here for convenience. Namely, the translational resistance tensor $\mathbb{A}$ is equal to:

$$A_{ij} \equiv A_\perp(\delta_{ij} - n_i n_j) + A_\parallel n_i n_j\,, \tag{A2}$$

where we recall that $\hat{\mathbf{n}}$ is a unit vector parallel to the axis of symmetry of the spheroid, and with coefficients

$$A_\perp = \frac{8(\beta^2-1)}{3\beta[(2\beta^2-3)\gamma+1]}\,, \quad A_\parallel = \frac{4(\beta^2-1)}{3\beta[(2\beta^2-1)\gamma-1]}\,, \quad \text{where } \gamma = \frac{\ln[\beta+\sqrt{\beta^2-1}]}{\beta\sqrt{\beta^2-1}}\,.$$

These expressions are consistent with those given in Tables 3.4 and 3.6 in Kim and Karrila (1991). In the case of interest here, the aspect ratio β is $\ll 1$, so $\gamma \approx \pi/(2\beta)$, $A_\perp \approx 16/(9\pi)$ and $A_\parallel \approx 8/(3\pi)$. This implies that in a still fluid, crystals settling with their maximal dimension oriented vertically are $3/2$ faster than crystals with their major axis oriented horizontally. Note that in a fluid at rest, only the horizontal configuration is stable.

The expression for the torque $\boldsymbol{\tau}_h^{(0)}$, named after Jeffery (Jeffery 1922), is:

$$\boldsymbol{\tau}^{(0)} = 6\pi a_\perp \mu\big[\mathbb{C}(\boldsymbol{\Omega}-\boldsymbol{\omega}) + \mathbb{H}:\mathbb{S}\big]\,. \tag{A3}$$

Here $\boldsymbol{\omega}-\boldsymbol{\Omega}$ is the angular slip velocity, and $\boldsymbol{\Omega} = \frac{1}{2}\boldsymbol{\nabla}\times\boldsymbol{u}$ is half the fluid vorticity at the particle position. It is related to the asymmetric part $\mathbb{O}$ of the matrix of fluid-velocity gradients by the relation $\mathbb{O}\boldsymbol{r} = \boldsymbol{\Omega}\times\boldsymbol{r}$. The symmetric part of the matrix of fluid-velocity gradients is denoted by $\mathbb{S}$. The resistance tensors $\mathbb{C}$ and $\mathbb{H}$ in Eq.(A3) have the following explicit expressions:

$$C_{ij} \equiv C_\perp(\delta_{ij} - n_i n_j) + C_\parallel n_i n_j\,, \quad H_{ijk} = H_0 \varepsilon_{ijl} n_k n_l\,, \tag{A4}$$

with

$$C_\perp = \frac{8a^2(\beta^4-1)}{9\beta[(2\beta^2-1)\gamma-1]}\,, \quad C_\parallel = -\frac{8a^2\beta(\beta^2-1)}{9(\gamma-1)\beta^2}\,, \quad H_0 = -C_\perp\frac{\beta^2-1}{\beta^2+1}\,.$$

Here ε_{ijl} is the antisymmetric tensor, and repeated indices are summed over.

b. Force and torque due to fluid inertia

The expressions of the contributions due to fluid inertia are estimated by considering a particle falling through a quiescent fluid with a steady settling velocity. The slip generates fluid accelerations, and acts as a homogeneous background flow. To leading order in the particle Reynolds number, the resulting steady convective-inertia corrections

to the force and torque in a quiescent fluid are (Brenner 1961; Cox 1965; Khayat and Cox 1989; Dabade et al. 2015):

$$\boldsymbol{f}^{(1)} = -(6\pi a_\perp \mu)\frac{3}{16}\frac{aW}{\nu}\left[3\mathbb{A} - \mathbb{I}\mathrm{d}(\hat{\boldsymbol{W}}\cdot\mathbb{A}\hat{\boldsymbol{W}})\right]\mathbb{A}\boldsymbol{W}, \tag{A5a}$$

$$\boldsymbol{\tau}^{(1)} = F(\beta)\mu\,\frac{a^3W^2}{\nu}\,(\hat{\boldsymbol{n}}\cdot\hat{\boldsymbol{W}})(\hat{\boldsymbol{n}}\times\hat{\boldsymbol{W}})\,. \tag{A5b}$$

Here $W = |\boldsymbol{W}|$ is the modulus of the slip velocity $\boldsymbol{W} = \boldsymbol{v} - \boldsymbol{u}$, $\hat{\boldsymbol{W}} = \boldsymbol{W}/W$ is its direction, $\mathbb{I}\mathrm{d}$ is the identity matrix, and $F(\beta)$ is a shape factor computed by Dabade et al. (2015). For oblate spheroids with $\beta \ll 1$, the shape factor $F(\beta)$ is positive, and tends to a finite limit of order ≈ 2.2 when $\beta \to 0$.

c. Moment of inertia tensor

The moment of inertia tensor of spheroids per unit mass, $\mathbb{I}$, is given by:

$$I_{ij} = I_\perp(\delta_{ij} - n_i n_j) + I_\parallel n_i n_j\,, \quad \text{with} \quad I_\perp = \frac{1+\beta^2}{5}a_\perp^2 \quad \text{and} \quad I_\parallel = \frac{2}{5}a_\perp^2\,. \tag{A6}$$

APPENDIX B

List of the runs

TABLE B1. Runs used to determine the collision properties between crystals. The flow properties are listed in Table 1. The number of crystals followed is N_c, T_{run} is the duration of the runs. The value of the averaged settling velocity is U_s. The table also lists the values of the Stokes number, St, and of the settling number, Sv, defined by Eq. (6). The rms of the fluctuations of orientation, $\langle\varphi^2\rangle^{1/2}_{\mathrm{DNS}}$, can be compared to the predictions from Gustavsson et al. (2021), $\langle\varphi^2\rangle^{1/2}_{\mathrm{stoch}}$. We note that this model neglects the corrections of the crystal velocity due to fluid inertia, which explains much of the difference between the values reported here. The collision kernel K, defined by Eq. (7), and the collision kernel K^0 in the hypothetical case in the absence of gravity, are listed in the last two columns.

Runs	Flows	β	N_c	T_{run} (s)	U_s (cm/s)	St	Sv	$\langle\varphi^2\rangle^{1/2}_{\mathrm{DNS}}$ (deg).	$\langle\varphi^2\rangle^{1/2}_{\mathrm{stoch}}$ (deg).	K (cm^3/s)	K^0 (cm^3/s)
1	I	0.005	100^3	98	1.84	$8.4\,10^{-3}$	4.89	12.7	14.9	$1.2\,10^{-4}$	$4.3\,10^{-5}$
2	I	0.01	100^3	112	3.08	$1.7\,10^{-2}$	9.78	3.13	3.21	$5.9\,10^{-5}$	$4.2\,10^{-5}$
3	I	0.02	70^3	126	5.48	$3.4\,10^{-2}$	19.6	0.99	1.07	$4.9\,10^{-5}$	$4.1\,10^{-5}$
4	II	0.005	100^3	24	2.12	$3.4\,10^{-2}$	2.44	39.7	39.8	$6.7\,10^{-4}$	$1.6\,10^{-4}$
5	II	0.01	70^3	30	3.50	$6.8\,10^{-2}$	4.89	13.7	14.3	$4.2\,10^{-4}$	$2.0\,10^{-4}$
6	II	0.02	70^3	36	5.78	0.135	9.78	4.05	4.33	$2.7\,10^{-4}$	$3.0\,10^{-4}$
7	II	0.05	70^3	31.5	11.5	0.338	24.5	4.05	5.05	$2.4\,10^{-4}$	$8.6\,10^{-4}$
8	III	0.005	100^3	5.28	2.4	0.134	1.23	54.3	55.4	$1.4\,10^{-3}$	$1.0\,10^{-3}$
9	III	0.01	100^3	5.28	4.5	0.268	2.45	38.0	41.5	$2.4\,10^{-3}$	$1.9\,10^{-3}$
10	III	0.02	100^3	5.28	7.4	0.536	4.91	19.8	21.1	$3.6\,10^{-3}$	$4.7\,10^{-3}$

APPENDIX C

Collision rate in the absence of gravity

Studying collisions in the absence of gravity is a very simplified problem, not obviously appropriate in an atmospheric science context, as it completely misses the differential settling mechanism, which was shown to play an important role in Section 3b. On the other hand, the simplification is helpful in elucidating the physical mechanisms responsible for collisions. Figure C1 shows the collision kernel, as defined in a particle suspension by Eq. (7), in the absence of gravitational settling (the values are listed as K^0 in Table B1). The dashed line in the figure shows the $\varepsilon^{1/2}$ behavior, corresponding to the Saffman-Turner prediction (Saffman and Turner 1956). The data indicates a $K^0 \approx \varepsilon^{1/2}$ behavior provided the Stokes number satisfies $\mathrm{St} \lesssim 0.1$, which is the case for all particles for $\varepsilon \approx 1\,\mathrm{cm}^2/\mathrm{s}^3$, and for particles with

$\beta \leq 0.01$ at $\varepsilon \approx 16\,\mathrm{cm}^2/\mathrm{s}^3$. When $\mathrm{St} \gtrsim 0.1$, clear deviations are visible. A similar picture was found in the case of colliding particles of spherical shapes (Voßkuhle et al. 2014).

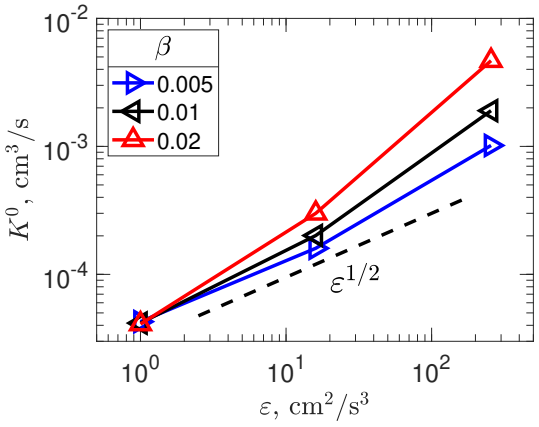

FIG. C1. Dependence of the collision kernel, in the absence of gravitational settling, on the energy dissipation, for $\beta = 0.005$ (right-pointing triangles), 0.01 (left-pointing triangles) and 0.02 (upper-pointing triangles). The dashed line corresponds to the dependence predicted in Saffman and Turner (1956), and provides a good description of the data when $\mathrm{St} \lesssim 0.1$.

References

Anand, P., S. S. Ray, and G. Subramanian, 2020: Orientation dynamics of sedimenting anisotropic particles in turbulence. *Phys. Rev. Lett.*, **125**, 034 501.

Ayala, O., B. Rosa, and L. Wang, 2008a: Effects of turbulence on the geometric collision rate of sedimenting droplets. part 2. theory and parametrization. *New J. Phys.*, **10**, 075 016.

Ayala, O., B. Rosa, L. Wang, and W. W. Grabowski, 2008b: Effects of turbulence on the geometric collision rate of sedimenting droplets. part 1. results from direct numerical simulations. *New J. Phys.*, **10**, 075 015.

Batchelor, G. K., and J. T. Green, 1972: Hydrodynamic interaction of two small freely-moving spheres in a linear flow field. *J. Fluid Mech.*, **56**, 375–400.

Brenner, H., 1961: The Oseen resistance of a particle of arbitrary shape. *J. Fluid Mech.*, **11**, 604–610.

Bréon, F.-M., and B. Dubrulle, 2004: Horizontally oriented plates in clouds. *Journal of the Atmospheric Sciences*, **61**, 2888–2898.

Cabrera, F., M. Z. Sheikh, B. Mehlig, N. Plihon, M. Bourgoin, A. Pumir, and A. Naso, 2022: Experimental validation of fluid inertia models for a cylinder settling in a quiescent flow. *Phys. Rev. Fluids*, **7**, 024 301.

Cheng, K.-Y., P. K. Wang, and T. Hashino, 2015: A numerical study on the attitudes and aerodynamics of freely falling hexagonal ice plates. *Journal of the Atmospheric Sciences*, **72 (9)**, 3685 – 3698.

Choi, Y. K., J. W. Wang, W. Wang, M. S. Kim, and G. Elbner, 2009: Continuous collision for ellipsoids. *IEEE Trans. Vis. Comput. Graphics*, **15**, 311–325.

Chun, J., D. L. Koch, S. L. Rani, A. Ahluwalia, and L. R. Collins, 2005: Clustering of aerosol particles in isotropic turbulence. *J. Fluid Mech.*, **536**, 219–251.

Connolly, P. J., C. Emersic, and P. R. Field, 2012: A laboratory investigation into the aggregation efficiency of small ice crystals. *Atmospheric Chemistry and Physics*, **12 (4)**, 2055–2076.

Cox, R., 1965: The steady motion of a particle of arbitrary shape at small Reynolds numbers. *J. Fluid Mech.*, **23**, 625–643.

Dabade, V., N. K. Marath, and G. Subramanian, 2015: Effects of inertia and viscoelasticity on sedimenting anisotropic particles. *J. Fluid Mech.*, **778**, 133–188.

Devenish, B. J., and Coauthors, 2012: Droplet growth in warm turbulent clouds. *Q. J. R. Meteorol. Soc.*, **138**, 1401–1429.

Elgobashi, S. E., 1994: On predicting particle-laden turbulent flows. *Applied Scientific Research*, **52**, 309–329.

Falkovich, G., A. Fouxon, and G. Stepanov, 2002: Acceleration of rain initiation by cloud turbulence. *Nature*, **419**, 151.

Falkovich, G., K. Gawedzki, and M. Vergassola, 2001: Particles and fields in fluid turbulence. *Rev. Mod. Phys.*, **73**, 913.

Falkovich, G., and A. Pumir, 2007: Sling effect in collisions of water droplets in turbulent clouds. *J. Atmos. Sci.*, **64**, 4497–4505.

Field, P. R., and A. J. Heymsfield, 2003: Aggregation and scaling of ice crystal size distributions. *J. Atmosphic Sci.*, **60**, 544–560.

Franklin, C. N., P. A. Vaillancourt, M. K. Yau, and P. Bartello, 2005: Collision rates of cloud droplets in turbulent flow. *J. Atmos. Sci.*, **62**, 2451–2466.

Gavze, E., and A. Khain, 2022: Gravitational collision of small non-spherical particles: swept volumes of prolate and oblate spheroids in calm air.

Good, G. H., P. J. Ireland, G. P. Bewley, E. Bodenschatz, L. R. Collins, and Z. Warhaft, 2014: Settling regimes of inertial particles in isotropic turbulence. *Journal of Fluid Mechanics*, **759**, R3, https://doi.org/10.1017/jfm.2014.602.

Grabowski, W. W., and P. Vaillancourt, 1999: Comments on "preferential concentration of cloud droplets by turbulence: Effects on the early evolution of cumulus droplet spectra". *J. Atmosphic Sci.*, **56**, 1433–1436.

Grabowski, W. W., and L. P. Wang, 2013: Growth of cloud droplets in a turbulent environment. *Ann. Rev. Fluid Mech.*, **45**, 293–324.

Gustavsson, K., J. Jucha, A. Naso, E. Lévêque, A. Pumir, and B. Mehlig, 2017: Statistical model for the orientation of nonspherical particles settling in turbulence. *Phys. Rev. Lett.*, **119**, 254 501.

Gustavsson, K., and B. Mehlig, 2011: Distribution of relative velocities in turbulent aerosols. *Phys. Rev. E*, **84**, 045 304.

Gustavsson, K., and B. Mehlig, 2016: Statistical model for collisions and recollisions of inertial particles in mixing flows. *The European Physical Journal E*, **39**, 55.

Gustavsson, K., B. Mehlig, and M. Wilkinson, 2008: Collisions of particles advected in random flows. *New J. Phys.*, **10**, 075 014.

Gustavsson, K., M. Z. Sheikh, D. Lopez, A. Naso, A. Pumir, and B. Mehlig, 2019: Theory for the effect of fluid inertia on the orientation of a small spheroid settling in turbulence. *New J. Phys.*, **21**, 083 008.

Gustavsson, K., M. Z. Sheikh, A. Naso, A. Pumir, and B. Mehlig, 2021: Effect of particle inertia on the alignment of small ice crystals in turbulent clouds. *J. Atmos. Sci.*, **78**, 2573–2587.

Hashino, T., M. Chiruta, D. Polzin, A. Kubicek, and P. K. Wang, 2014: Numerical simulation of the flow fields around falling ice crystals with inclined orientation and the hydrodynamic torque. *Atmospheric Research*, **150**, 79–96.

Hosler, C. L., and R. E. Hallgren, 1960: The aggregation of small ice crystals. *Discuss. Faraday Soc.*, **30**, 200–207.

Ireland, P., A. Bragg, and L. Collins, 2016: The effect of Reynolds number on inertial particle dynamics in isotropic turbulence. Part 2. Simulations with gravitational effects. *J. Fluid Mech.*, **796**, 659–711.

Jeffery, G. B., 1922: The motion of ellipsoidal particles immersed in a viscous fluid. *Proc. R. Soc. A*, **102**, 161.

Jiang, F., L. Zhao, H. Andersson, K. Gustavsson, A.Pumir, and B. Mehlig, 2021: Inertial torque on a small spheroid in a stationary uniform flow. *Phys. Rev. Fluids*, **6**, 024 302.

Jiang, Z., J. Verlinde, E. E. Clothiaux, K. Aydin, and C. Schmitt, 2019: Shapes and fall orientations of ice particle aggregates. *J. Atmospheric Sci.*, **76**, 1903–1916.

Jost, A., M. Szakáll, K. Diehl, S. K. Mitra, A. Hudertmark, B. S. Klug, and S. Borrmann, 2019: The effect of turbulence on the accretional growth of graupels. *J. Atmospheric Sci.*, **76**, 3047–3061.

Jucha, J., A. Naso, E. Lévêque, and A. Pumir, 2018: Settling and collision between small ice crystals in turbulent flows. *Phys. Rev. Fluids*, **3**, 014 604.

Keith, W., and C. Saunders, 1989: The collection efficiency of a cylindrical target for ice crystals. *Atmospheric Research*, **23 (1)**, 83–95.

Khain, A., and M. Pinsky, 2018: *Physical processes in clouds and cloud modeling*. Cambridge University Press, Cambridge, UK.

Khayat, R., and R. Cox, 1989: Inertia effects on the motion of long slender bodies. *J. Fluid Mech.*, **209**, 435–462.

Kim, S., and S. J. Karrila, 1991: *Microhydrodynamics: principles and selected applications*. Butterworth-Heinemann, Boston.

Klett, J. D., 1995: Orientation model for particles in turbulence. *J. Atmospheric Sci.*, **52**, 2276–2285.

Kramel, S., 2017: Non-spherical particle dynamics in turbulence. Ph.D. thesis, Wesleyan University.

Lo, K. K., and R. E. Passarelli, 1982: The growth of snow in winter storms: an airborne observational study. *J. Atmos. Sci.*, **39**, 697–706.

Lopez, D., and E. Guazzelli, 2017: Inertial effects on fibers settling in a vortical flow. *Phys. Rev. Fluids*, **2**, 024 306.

Magnusson, G., A. Dubey, R. Kearney, G. P. Bewley, and B. Mehlig, 2021: Collisions of micron-sized, charged water droplets in still air. 2106.11543.

Matrosov, S. Y., R. F. Reinking, and I. V. Djalalova, 2005: Inferring fall attitudes of pristine dendritic crystals from polarimetric radar data. *Journal of the Atmospheric Sciences*, **62 (1)**, 241 – 250, https://doi.org/10.1175/JAS-3356.1.

Maxey, M. R., 1987: The gravitational settling of aerosol particles in homogeneous turbulence and random flow fields. *J. Fluid Mech.*, **174**, 441–465.

Menon, U., A. Roy, S. Kramel, G. Voth, and D. Koch, 2017: Theoretical predictions of the orientation distribution of high-aspect-ratio, inertial particles settling in isotropic turbulence. *Abstract Q36.00011, 70th Annual Meeting of the APS Division of Fluid Dynamics, Denver, Colorado*.

Mitchell, D. L., 1988: Evolution of snow-size spectra in cyclonic storm. part i: Snow growth by vapor deposition and aggregation. *J. Atmos. Sci.*, **45**, 3431–3451.

Nakaya, U., and T. J. Terada, 1935: Simultaneous observations of the mass, falling velocity and form of individual snow crystals. *J. Fac. Sci. Hokkaido Imp. Univ. Ser.*, **1 (7)**, 191–200.

Naso, A., J. Jucha, E. Lévêque, and A. Pumir, 2018: Collision rate of ice crystals with water droplets in turbulent flows. *Journal of Fluid Mechanics*, **845**, https://doi.org/10.1017/jfm.2018.238.

Nettesheim, J. J., and P. K. Wang, 2018: A numerical study on the aerodynamics of freely falling planar ice crystals. *Journal of the Atmospheric Sciences*, **75 (9)**, 2849 – 2865, https://doi.org/10.1175/JAS-D-18-0041.1.

Nielsen, P., 1993: Turbulence effects on the settling of suspended particles. *Journal of Sedimentary Research*, **63 (5)**, 835–838.

Pitter, R. L., H. R. Pruppacher, and A. E. Hamielec, 1973: A numerical study of viscous flow past a thin oblate spheroid at low and intermediate reynolds numbers. *Journal of Atmospheric Sciences*, **30 (1)**, 125 – 134.

Pruppacher, H. R., and J. D. Klett, 1997: *Microphysics of clouds and precipitation, 2nd edition*. Kluwer Academic Publishers, Dordrecht, The Nederlands, 954p.

Pumir, A., and M. Wilkinson, 2016: Collision aggregation due to turbulence. *Ann. Rev. Cond. Matt. Phys.*, **7**, 141.

Rosa, B., H. Parishani, O. Ayala, and L.-P. Wang, 2016: Settling velocity of small inertial particles in homogeneous isotropic turbulence from high-resolution DNS. *International Journal of Multiphase Flow*, **83**, 217 – 231.

Saffman, P. G., and J. S. Turner, 1956: On the collision of drops in turbulent clouds. *J. Fluid Mech.*, **1**, 16–30.

Saito, I., and T. Gotoh, 2019: Turbulence and cloud droplets in cumulus clouds. *New J.. Phys.*, **20 (2)**, 023 001.

Shaqfeh, E. S. G., and D. L. Koch, 1990: Orientational dispersion of fibers in extensional flows. *Physics of Fluids A: Fluid Dynamics*, **2 (7)**, 1077–1093.

Shaw, R. A., 2003: Particle-turbulence interactions in atmospheric clouds. *Annu. Rev. Fluid Mech.*, **35**, 183.

Sheikh, M. Z., K. Gustavsson, D. Lopez, E. Leveque, B. Mehlig, A. Pumir, and A. Naso, 2020: Importance of fluid inertia for the orientation of spheroids settling in a turbulent flow. *J. Fluid Mech.*, **886**, A9–15.

Shima, S., Y. Sato, A. Hashimoto, and R. Misumi, 2020: Predicting the morphology of ice particles in deep convection using the super-droplet method: development and evaluation of scale-sdm 0.2.5-2.2.0, -2.2.1, and -2.2.2. *Geoscientific Model Development*, **13 (9)**, 4107–4157.

Siewert, C., R. P. J. Kunnen, M. Meinke, and W. Schröder, 2014a: Orientation statistics and settling velocity of ellipsoids in decaying turbulence. *Atmos. Res.*, **142**, 45–56.

Siewert, C., R. P. J. Kunnen, and W. Schrőder, 2014b: Collision rates of small ellipsoids settling in turbulence. *J. Fluid Mech.*, **758**, 686–701.

Sundararajakumar, R. R., and D. L. Koch, 1996: Non-continuum lubrication flows between particles colliding in a gas. *Journal of Fluid Mechanics*, **313**, 283–308, https://doi.org/10.1017/S0022112096002212.

Voßkuhle, M., E. Lévêque, M. Wilkinson, and A. Pumir, 2013: Multiple collisions in turbulent flows. *Phys. Rev. E*, **88**, 063 008.

Voßkuhle, M., A. Pumir, E. Lévêque, and M. Wilkinson, 2014: Prevalence of the sling effect for enhancing collision rates in turbulent suspensions. *J. Fluid Mech.*, **749**, 841.

Wang, L., and M. R. Maxey, 1993: Settling velocity and concentration distribution of heavy particles in homogeneous isotropic turbulence. *J. Fluid Mech.*, **256**, 27–68.

Wang, L. P., O. Ayala, S. E. Karprzak, and W. W. Grabowski, 2005: Theoretical formulation of collision rate and collision efficiency of hydrodynamically interacting cloud droplets in turbulent atmosphere. *J. Atmos. Sci.*, **62**, 2433.

Wang, L. P., A. S. Wexler, and Y. Zhou, 1998: On the collision rate of small particles in isotropic turbulence. i. zero inertia case. *Phys. Fluids*, **10**, 266–76.

Wang, P. K., 2013: *Physics and Dynamics of Clouds and Precipitation*. Cambridge University Press, https://doi.org/10.1017/CBO9780511794285.

Wang, P. K., and W. Ji, 1997: Numerical simulation of three-dimensional unsteady flow past ice crystals. *Journal of the Atmospheric Sciences*, **54 (18)**, 2261 – 2274.

Wilkinson, M., and B. Mehlig, 2005: Caustics in turbulent aerosols. *Europhys. Lett.*, **71**, 186–192.

Wilkinson, M., B. Mehlig, and V. Bezuglyy, 2006: Caustic activation of rain showers. *Phys. Rev. Lett.*, **97**, 048 501.

Willmarth, W. W., N. E. Hawk, and R. L. Harvey, 1964: Steady and unsteady motions and waks of freely falling disks. *Phys. Fluids*, **7**, 197–208.

Yang, P., K. N. Liou, L. Bin, and B. A. Baum, 2015: On the radiative properties of ice clouds: Light scattering, remote sensing and radiation parametrization. *Adv. Atmos. Sci.*, **32**, 32–63.